



Tsunami intensity scale based on wave amplitude and current applied to the French Riviera: the case study of local seismicity

Laurie Boschetti¹ · Mansour Ioualalen¹ · Fatemeh Nemati² · Stephan Grilli² · Jean-Xavier Dessa¹ · Christophe Larroque¹

Received: 4 November 2019 / Accepted: 4 April 2020 / Published online: 18 April 2020
© Springer Nature B.V. 2020

Abstract

The French–Italian Riviera faces several geophysical hazards, including recurrent earthquakes and underwater landslides that can be tsunamigenic. The stakes are high since this is a densely populated and touristic area. Several studies have already been carried out, in particular to map tsunami hazard resulting from the near-field seismicity of the North Ligurian Faults System, which is located a short distance off the coast. In our most recent study, runup maps were developed together with local analyses of tsunami-induced current fields. However, no conclusions were drawn, based on these results, as of the associated tsunami risk along the coast. Here, to this effect, we apply a recently proposed tsunami intensity scale to the simulation results obtained in our previous work (maximum values of tsunami depths and currents). This intensity scale (7 levels) is mapped over the entire coastal area, and its site-specific values are discussed. The scale allows quantifying the potential damage inland and at sea, based on a standard coastal vulnerability that has been assessed through different records. It thus represents a useful tool to help improving our preparedness to tsunami hazard.

Keywords French Riviera · 1887 Earthquake · Tsunami intensity · Funwave

1 Introduction

The Ligurian basin is one of the most seismically active zones in Western Europe (Béthoux et al. 1992; Eva et al. 2001; Larroque et al. 2001) and includes the North Ligurian Faults System (NLFS) (Larroque et al. 2011), which has an estimated 80 km length in a N 55 °E orientation (NE-SW). At shallow depth, this fault system does not appear as a single continuous fault, but instead as a network of active reverse fault branches (Figs. 1, 2). At larger

✉ Mansour Ioualalen
Mansour.Ioualalen@geoazur.unice.fr

¹ Observatoire de la Côte d’Azur, CNRS, IRD, Géoazur, Université Côte d’Azur, Campus Azur, 250 rue Albert Einstein, CS 10269, 06905 Sophia Antipolis Cedex, France

² Department of Ocean Engineering, Graduate School of Oceanography, University of Rhode Island, Sheets Building 215, Narragansett, RI 02882, USA

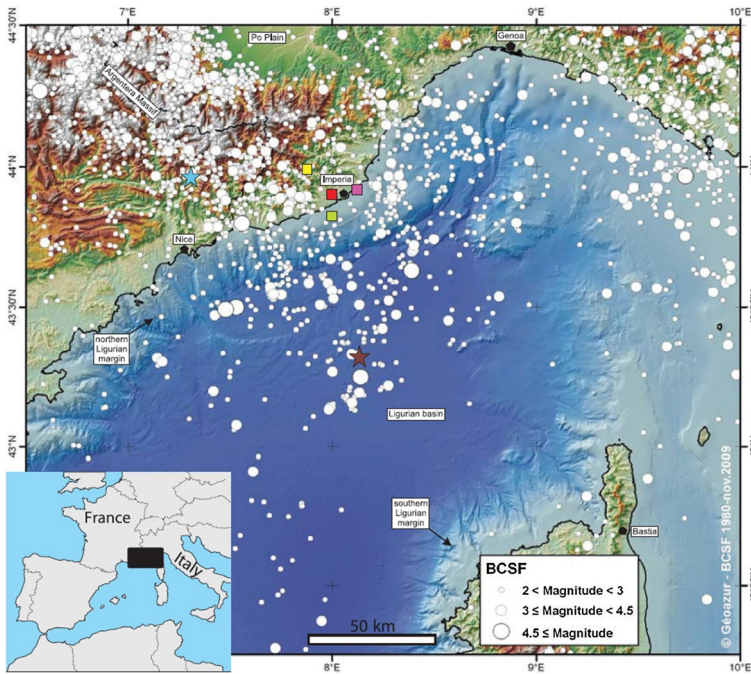


Fig. 1 Seismicity map of the Ligurian area during the period 1880–2010 (Catalog of the Bureau Central Sismologique Français, <https://www.franceseisme.fr/>). The compilation is obtained from various sources: the French Institut Géographique National (IGN), the Shuttle Radar Topography Mission (SRTM, NASA), and the French Institut Français de Recherche et d'Exploration de la Mer (IFREMER). Magnitudes range from Mw2 to Mw4.7. The coloured stars correspond to estimated epicentres of July 20, 1564 (blue star), and July 19, 1863 (brown star), earthquakes. Colored squares are the former estimated epicentres of the February 27, 1887 event (prior to analyses by Larroque et al. 2012; Ioualalen et al. 2014)

depth, however, it is not known whether these shallow strands merge. Figure 2 shows the location of the Ligurian faults system and associated bathymetry, which extends along the French–Italian Riviera, thus exposing these territories to potential seismic and tsunami hazards.

During the past half-millennium, a dozen local tsunamis have been reported in the area (Tinti et al. 2004; Lambert and Terrier 2011), most of these having most likely been triggered by earthquakes. Most of the historical local earthquakes have been of moderate magnitude (up to M_w 5 or so; Béthoux et al. 1992; Larroque et al. 2009), with the notable exception the large event that occurred on February 23, 1887 (Ferrari 1991; Eva and Rabinovich 1997; Larroque et al. 2012), offshore Imperia (Italian Riviera). Based on a careful analysis of a tide gauge record at Genoa, Italy, Larroque et al. (2012) and Ioualalen et al. (2014) estimated this event magnitude to be in the M_w 6.7–6.9 range. This estimate was also based on: (1) an analysis of the marine geophysical data, showing the existence of an active faults system at the foot of the Ligurian margin (Larroque et al. 2011), and (2) the analysis of macroseismic historical databases, using several models of intensity attenuation with distance and focal depth, as well as the modeling of the tsunami induced by the 1887 Ligurian earthquake (runups and their distribution documented in the historical archives). This joint seismotectonic–macroseismic–tsunami modeling study helped Larroque et al.

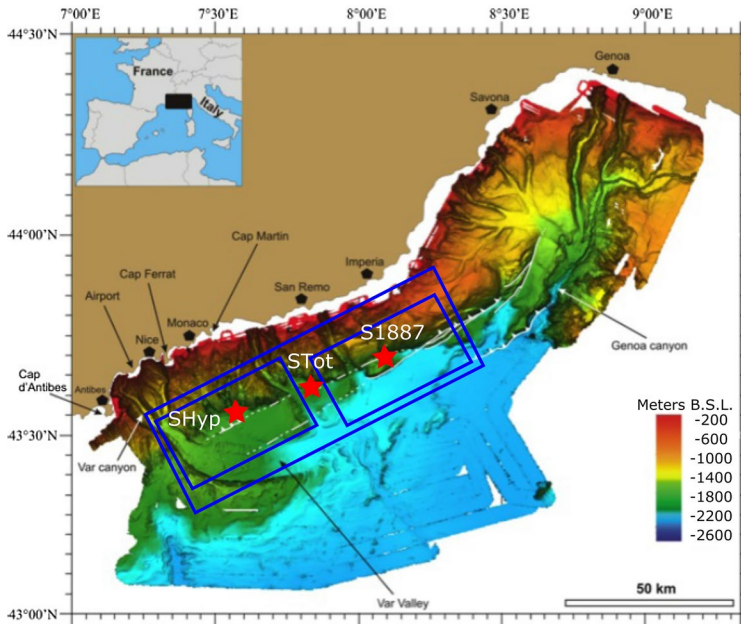


Fig. 2 The 80-km long North Ligurian Faults System, NLFS (in white at the toe of the continental slope) and the bathymetry of the region (MALISAR research cruises). Centroids (red stars) and ruptured areas (blue rectangles) are represented for scenarios S1887, SHyp and STot (Table 2)

(2012) and Ioualalen et al. (2014) specifying the location, kinematics, and magnitude of the earthquake (20–30 km offshore of the Imperia coast, focal depth 15 km, reverse faulting and M_w 6.7–6.9) and to discuss scenarios for future potential seismic/tsunami events in this area (Nemati et al. 2019). Using a different approach and intensity attenuation model, a recent study was conducted on historical seismicity based on intensity prediction equations (IPE), which confirmed a M_w 6.7–6.8 magnitude for the 1887 Ligurian earthquake (Manchuel et al. 2017).

The 1887 earthquake caused about 600 fatalities (Denza 1887; Taramelli and Mercalli 1888) and triggered a tsunami with up to 1–2 m runups measured from Antibes, France, to Albenga, Italy. Therefore, this historical event, and other similar or even larger events that may have occurred prior to it, can serve as reference extreme events to assess tsunami hazard along the Ligurian coast.

The tsunami hazard in the Ligurian region, and more particularly along the French Riviera, has already been addressed in several studies. Ioualalen et al. (2014) analyzed the tsunamigenic potential stemming from underwater mass wasting events, and Ioualalen et al. (2010) and Nemati et al. (2019), extended the earlier analysis to near-field coseismic tsunamis. Regarding far-field coseismic tsunamis, on the southern coast of the Mediterranean Sea, the seismotectonic context of the Algerian margin is similar to the Ligurian one (Déverchère et al. 2005). For instance, the Boumerdes earthquake (2003/05/21, M_w 6.8) nucleated on an offshore south dipping reverse fault and produced a tsunami that crossed the western Mediterranean. It reached the southern coast of France ~90 min after the earthquake occurrence time. The sea elevation measured at tide gages varied by location and was on the order of tens of centimeters (Alasset et al. 2006; Sahal et al. 2009). Although the seismic activity is greater on the Algerian margin (more frequent earthquakes, higher

magnitudes), the consequences for the Ligurian margin remain moderate due to tsunami attenuation with distance and travel time required for the waves to cross the Mediterranean.

While Ioualalen et al. (2014) used fairly coarse grids (100 m resolution), Nemati et al. (2019) carried out computations in increasingly finer nested grids (down to 40 m or even 10 m) and, besides tsunami elevation and runups, discussed the induced tsunami currents. Recent studies of tsunami hazard along the United States east coast have recommended the use of grids of at least 30 m resolution, in order to get converged currents and inundation maps in model simulations (Grilli et al. 2015; Schambach et al. 2018). Our simulations here, as well as those of Nemati et al. (2019), were conducted within this range of grid resolution.

The present study is based on more accurate and detailed runup maps, maximum tsunami depths, and currents than in the previous studies. But, more importantly, it extends the mere mapping of tsunami hazard done in earlier work by establishing, for the first time in the Ligurian area, tsunami intensity maps that allow assessing the associated tsunami risk. The latter maps are based on the tsunami intensity scale recently proposed by Boschetti and Ioualalen (2019, submitted) (hereafter BI-20), which allows assessing and thus anticipating possible damage that earthquake-induced tsunamis would cause. Thanks to this new step, the local tsunami maximum depth and current values can be placed in a more general context, to quantify the tsunami risk along this coastal area.

2 Methodology

We follow the standard procedure in coseismic tsunami modeling, consisting in: (1) building a computational grid over an accurate bathymetry/topography digital elevation model (DEM), (2) for selected hypothetical events (earthquake scenarios), computing the coseismic seafloor deformation using the Okada (1985) half-space dislocation model, (3) using this deformation as initial condition in a long wave model, computing the tsunami propagation to shore within the grid over a certain time duration, and (4) based on results, mapping runups, maximum tsunami depth (H_{\max}), and maximum currents (CUR_{\max}). Following BI-20, H_{\max} is defined as the maximum inland inundation depth, that is flow depth over grade (calculated as tsunami surface elevation over mean sea level minus the local land elevation). As mentioned by BI-20, this definition of H_{\max} is coherent for defining an intensity scale because the effect of a tsunami on a structure depends on the water column depth along the structure (and corresponding induced current). The tsunami intensity maps obtained this way will be discussed in a site-specific manner. Each of the steps in our methodology is detailed below.

2.1 The tsunami intensity scale

BI-20 proposed a tsunami intensity scale I_T that was specially designed for numerical simulations. The scale is function of the tsunami magnitude M_T and the biophysical vulnerability VB_T of the impacted areas: $I_T = f(M_T, VB_T)$ [their Eq. (1)]. The intensity corresponds to the effects and impacts of the considered physical event on (static or moving) structures, human losses, and on the environmental changes (Papadopoulos 2003). Tsunami magnitude is function of the physical parameters of the tsunami, such as maximum currents CUR_{\max} and tsunami amplitude H_{\max} , which are typically obtained as outputs of numerical simulations. Nowadays, currents are also systematically analyzed in tsunami studies because

they impede navigation and can be extremely damaging to floating or anchored marine structures in harbors. Tsunami induced currents, which are fairly uniform over depth, may cause large momentum and drag forces and even transform into dangerous eddies around sharp marine structures. The biophysical vulnerability is related to the preparedness of the community against the considered physical hazard. BI-20s intensity scale was derived following a careful analysis of (CUR_{max} , H_{max}) values, along with a comprehensive integration of pre-existing tsunami scales or analyses (Fig. 3, Table 1). It is inspired by the magnitude scale that was developed by the French authorities based on decades of observations of numerous yearly flooding in French rivers. It serves as the basis for the French Prevention Plan against Flooding Risk (PPFR) (PPFR 1999; PPFR-Thau 2012), and it is based on the effects of both the actual water level and the current during river floods. The application of this approach to tsunamis follows from the following observations: (a) being a long wave, the current induced by a tsunami may be considered to be nearly horizontal and uniform within the water column. Thus, the tsunami flow is similar to flooding; (b) PPRFs refer to the terminology “*water level*” corresponding to the water column depth, that is the tsunami maximum amplitude H_{max} defined above. Based on the PPRF magnitude, BI-20 built their tsunami intensity scale by integrating biophysical vulnerability data proposed in other studies: some of these taking into account the effect of H_{max} only (Papadopoulos and Imamura 2001; Shuto 1991); others like Lynett et al. (2014)’s analysis only considering tsunami currents CUR_{max} .

Note that, with BI-20s index, one cannot really assess the vulnerability of society because only a median vulnerability is included in the intensity scale. Obviously, community preparedness against tsunami hazard is a key aspect that is inhomogeneous along the coast and can modify the tsunami intensity. Being prepared also includes the mitigating

Fig. 3 Tsunami intensity scale proposed by Boschetti and Ioualalen (2019, submitted). Their intensity is defined as a function of the magnitude [H_{max} (m) and CUR_{max} ($m\ s^{-1}$)] (see Table 1). The black, gray, and white lines represent the limits of movement in an upright position of a child or elderly, a non-sporty adult, and a sporty adult under stress, respectively

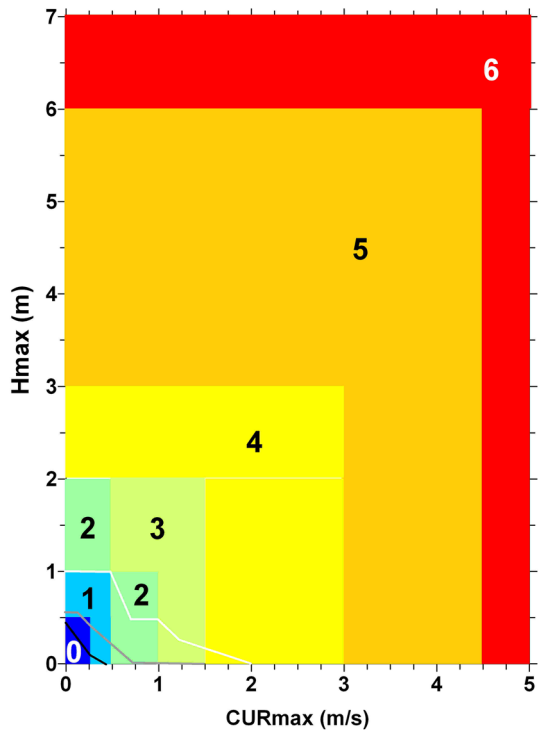


Table 1 Tsunami intensity scale proposed by Boschetti and Ioualalen (2019, submitted) (see Fig. 3 for H_{max} and CUR_{max} levels)

Tsunami intensity	Human damage on land (PPFR 1999; PPRF-Thau 2012; Papadopoulos and Imamura 2001)	Damage on land (Shuto 1991; Papadopoulos and Imamura 2001)	Damage at sea (Lynett et al. 2014; Table 2; Papadopoulos and Imamura 2001)	Tsunami perception (Lynett et al. 2014; Table 2; Papadopoulos and Imamura 2001)	Territorial management, prevention (Table 3) (PPFR 1999; PPRF-Thau 2012)
0	Possible upright displacement but children and older people may face difficulties	No damage	No damage to marine structures	None felt	–
1	Very difficult displacement for children and the elderly and difficult for a non-sporty adult Very low probability of victims	No damage	No damage to marine structures	At sea: small buoys moved Felt by few to most people on board small vessels Possibly observed on land	Caution areas: limit urban or agricultural development as much as possible Setting up a monitoring system; public information meetings; hazard mapping
2	No possible displacement for a child or a senior, very difficult for a non-sporty adult and difficult for a sporty adult Increased number of potential victims	No damage	No damage to marine structures Few small vessels move slightly onshore	At sea: small buoys moved Felt by all on board small vessels and by few people on board large vessels Observed by most people on land	Danger zones: prohibit urban and agricultural development Setting up a monitoring system; hazard mapping; set up an evacuation plan
3	No possible displacement for a child or senior, nearly impossible for a non-sporty adult and very difficult for a sporty adult Increased number of potential victims	Limited flooding of outdoor facilities (gardens) and near-shore facilities Limited flooding of cultivated land Traces of sand layer are left behind	Nearly no damage to marine structures (few boat shocks) Some small vessels move onshore	At sea: small buoys moved Felt by all on board large vessels Observed by all on the coast Few people are frightened and run to higher ground	Danger zones: prohibit urban or agricultural development. Remove as much existing development as possible Setting up a monitoring system; public information meetings; hazard mapping; set up an evacuation plan; construction of defense works against hazard (dikes) or re-naturalizing the environment (mangroves, bank vegetation, etc.)

Table 1 (continued)

Tsunami intensity	Human damage on land (PPFR 1999; PPRF-Thau 2012; Papadopoulos and Imamura 2001)	Damage on land (Shuto 1991; Papadopoulos and Imamura 2001)	Damage at sea (Lynett et al. 2014; Table 2; Papadopoulos and Imamura 2001)	Tsunami perception (Lynett et al. 2014; Table 2; Papadopoulos and Imamura 2001)	Territorial management, prevention (Table 3) (PPFR 1999; PPRF-Thau 2012)
4	Standing almost impossible for all people; ability to move while swimming if the current is not too strong Possible impacts with small drifting objects Increased number of potential victims because of greater numbers in the raised area	Damage and flooding in a few to many wooden structures Most masonry buildings withstand grade 1 damage Objects of variable size and instability overturn and drift Few aquaculture rafts washed away Sand layers and pebble accumulation	1–2 docks/small boats to moderate dock boat damage (<25% of docks/vessels damaged) and/or mid-sized vessels off moorings damaged Most small vessels move violently onshore	At sea: large buoys moved Most people are frightened and run to higher ground	
5	Standing impossible for all people; ability to move while swimming if the current is not too strong Few to many people are washed away Possible impacts with big drifting objects Increased number of potential victims because of greater numbers in the raised area	Beach erosion. Extensive flooding. Slight damage in tsunami control forest, stop drifts. Many aquaculture rafts washed away, few partially damaged Most wooden structures are washed away or demolished Damage of grade 2 to 3 in a few masonry buildings. Most RC buildings sustain damage, a few sustain flooding of grade 1 to 2, and flooding is observed	Moderate to major dock boat damage (<50% of docks/vessels damaged) and/or mid-sized to large vessels off moorings damaged Most large vessels move violently onshore	At sea: large buoys moved All people escape to higher ground	

Table 1 (continued)

Tsunami intensity	Human damage on land (PPFR 1999; PPRF-Thau 2012; Papadopoulos and Imamura 2001)	Damage on land (Shuto 1991; Papadopoulos and Imamura 2001)	Damage at sea (Lynett et al. 2014; Table 2; Papadopoulos and Imamura 2001)	Tsunami perception (Lynett et al. 2014; Table 2; Papadopoulos and Imamura 2001)	Territorial management, prevention (Table 3) (PPFR 1999; PPRF-Thau 2012)
6	Standing impossible for all people; ability to move while swimming if the current is not too strong Most to all people are washed away Increased number of potential victims because of greater numbers in the raised area	Cars overturned and drifted, oil spills, fires start Damage of grade 4 to 5 in many masonry buildings. Few to many RC buildings suffer damage of grade 3 to 5	Major to extreme dock/off-mooring boat damage (> 50% of vessels damaged) -Many collide with buildings	At sea: large buoys moved General panic	

influence of warning and evacuation plans. Each territory has its particularities, and that is why the scale intensity scale of BI-20 is only the first step towards tsunami hazard assessment, a first-order one or a mean state, which certainly could be improved by factoring in site-specific vulnerability or preparedness aspects.

2.2 Numerical model, computational grid and validation

Tsunami simulations are performed with *FUNWAVE*, a fully nonlinear and dispersive Boussinesq wave model (Wei and Kirby 1995; Wei et al. 1995), which was later parallelized by Pophet et al. (2011). A computational grid with a 40 m horizontal resolution was built in the coastal area ranging from Fréjus, France, to Imperia, Italy, and encompassing the Ligurian Faults System (Fig. 2). The domain is bounded by coordinates (6.80 °E to 8.57 °E; 43.19 °N to 43.95 °N) and has a 3565×2096 mesh size. An optimal time step of 0.075 s was chosen, to avoid numerical instabilities. Bathymetric and topographic data were obtained from various sources and interpolated to build a 10 m grid along the French Riviera; these data sets are thoroughly described in Nemati et al. (2019). In their tsunami simulations, Nemati et al. (2019) used *FUNWAVE-TVD*, a more recent version of *FUNWAVE* that has the ability of using nested grids and provide a model resolution commensurate with a finer bathymetry, where needed. The nested grid approach allows for an accurate modeling while keeping the computational effort manageable, as opposed to using a fine constant-mesh grid over the entire area. As a point of comparison, our simulations with *FUNWAVE* using a uniform 40 m resolution grid, for 1h30 of tsunami propagation, took 1 week of CPU time using a 8-core cluster, while it took only a few hours for Nemati et al. (2019) using *FUNWAVE-TVD* with much smaller nested grids, using a 24-core cluster. However, the effective times required to compile the simulations are quite comparable when one takes into account the preliminary grid processing required by *FUNWAVE-TVD* to nest their various successive computational domains of approximate resolutions 640 m, 160 m and 40 m. Nemati et al. (2019) performed further simulations in 10 m resolution grids and evaluated performance indices (*Norm*, *Determination coefficient*) and basic statistics (*mean*, *STD*, *cross-correlation*) for simulations at different resolutions. They concluded that their 10 m and 40 m results were in very good agreement with those obtained with *FUNWAVE* in a 40 m grid resolution (Nemati et al. 2019).

2.3 Coseismic tsunami sources

Similarly to Ioualalen et al. (2014) and Nemati et al. (2019), we assess tsunami hazard along the French Riviera resulting from local seismicity and the potential activation in future earthquakes of the NLFS (Fig. 2). We base our work on the earthquake scenarios first proposed by Larroque et al. (2012) and refined by Ioualalen et al. (2014) (Fig. 2, Table 2). These references provide discussions of the NLFS geological and seismotectonic contexts and of 3 proposed representative rupture scenarios: (1) S1887 (Larroque et al.'s 2012, S7 scenario), a M_w 6.91 rupture of the eastern NLFS segment, which is the likeliest scenario for the 1887 earthquake; (2) SHyp (Larroque et al.'s 2012, S8 scenario), a hypothetical event of similar parameters, but with its centroid shifted westward within the NLFS, offshore of the French–Italian border, which emulates the potential rupture of the NLFS western segment; (3) STot (Larroque et al.'s 2012, S11 scenario), an hypothetical extreme M_w 7.51 event, corresponding to the complete rupture of the 80 km–long NLFS. Some of the constitutive parameters for the latter event, i.e., the fault length and slip, were

Table 2 Rupture scenarios and parameters proposed and processed by Larroque et al. (2012) for the Northern Ligurian faults system (Fig. 2)

Scenario	X_0	Y_0	d (km)	ϕ	δ	λ	L (km)	W (km)	Δ (m)	M_w
S1887	43.7 °N	8.08 °E	15	235°	16°	90°	35	17	1.5	6.91
S_{Hyp}	43.58 °N	7.55 °E	15	235°	16°	90°	35	17	1.5	6.91
S_{Tot}	43.64 °N	7.815 °E	15	250°	16°	90°	80	27	3.3	7.51

Scenarios S1887, SHyp and STot correspond to their S7, S8 and S11 ones, respectively: centroid position (X_0 , Y_0) and depth d ; strike angle ϕ (counted CW from north); dip angle δ , rake angle λ , length and width of the ruptured area (L , W); amount of slip Δ , derived magnitude M_w .

derived from the seismic scaling laws of Wells and Coppersmith (1994) based on the fault length. It should be noted that tectonic motions and seismicity along the NLFS are closely monitored: along the Ligurian coast, dense networks of seismic stations are managed by French and Italian institutions, RESIF (*Réseau Sismologique et Géodésique Français*, <https://rlbp.resif.fr/spip.php?article30>), and RSNI (Regional Seismic Network of Northern Italy, <https://www.distav.unige.it/rsni/>). Despite the lack of permanent OBS (Ocean Bottom Seismometers), these networks allow for a real time detection of moderate ($M_w > 3$) and strong earthquakes both on- and off-shore. All these data are used by the institutions in charge of the tsunami warning procedures, i.e., the CENALT (*Centre d'Alerte aux Tsunamis*, <https://www.info-tsunami.fr/>), and the NEAMTWS (North Eastern Atlantic-Mediterranean Tsunami Warning System, <https://neamtic.ioc-unesco.org/>).

Based on our present knowledge of this fault system, the SHyp and STot scenarios appear quite plausible (Larroque et al. 2012), although no historical occurrence of such events has been documented, considering that the region has been populated very early in human history and that there are reliable historical archives dating back more than 10 centuries (Stucchi et al. 2012; Manchuel et al. 2017).

2.4 Initial surface elevations

The initial coseismic surface elevations computed for each scenario have a 0.34–1.12 m maximum elevation and a 0.13–0.45 m maximum depression (Fig. 4). This asymmetry in the maximum and minimum surface elevations results from a nonzero dip angle (Okada 1985). Based on the distributions of surface elevations shown in Fig. 4, we see that for scenario S1887, the Italian Riviera will first experience a sea withdrawal (leading depression wave). For the SHyp scenario, this will be the case for the area of the French Riviera near the Italian border (east of Nice) and for STot, both sides of the border will experience a sea withdrawal before the arrival of a tsunami crest. Elsewhere, these maps cannot tell how the tsunamis will first impact the coast because this will depend on wave spreading during propagation, which is depth dependent (e.g., there is a reduced spreading in the vicinity of the coast due to the shallow depth). In addition, the shallow initial wave troughs (between 0.13 and 0.45 m) indicate that there should be a limited sea withdrawal for these NLFS scenarios, which would probably be imperceptible, even though the leading depression waves will be amplified at the coast due to shoaling (approximately following Green's law, as a power $\frac{1}{4}$ of the water depths ratio), but in a very weak way as they are initiated in already fairly shallow waters.

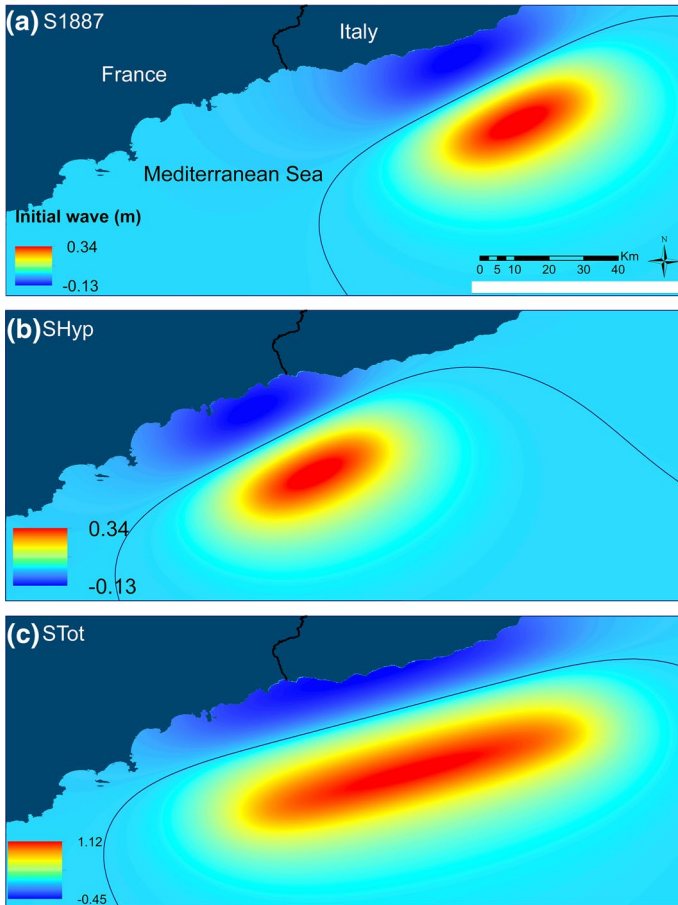


Fig. 4 Coseismic tsunami source elevation computed using Okada's (1985) method for rupture scenarios: S1887 (a); SHyp (b); and STot (c) (Fig. 2; Table 2). Positive elevation of the sea level corresponds to sea-floor uplift and negative elevation (i.e., depression) to subsidence. The black curves represent the nodal points (zero-elevation)

3 Simulation results

3.1 Overall tsunami runup variation along the French Riviera

Although scenarios (S1887, SHyp) and STot have very different moment magnitudes, with the extreme scenario having about 8 times the energy of the other 2 scenarios, their runup distributions exhibit very similar patterns along the coast (Fig. 5). This results from bathymetrically controlled long wave refraction over the continental slope and shelf, leading to identical patterns of wave focusing/defocusing for each tsunami (e.g., Tehranirad et al. 2015), and of similar bay resonances; however, as expected from the different source magnitude and location, maximum runup values significantly vary from one scenario to another (approximately from 1 to 7 m).

As shown in Fig. 5, in most bays, the isobaths are convex (relatively to a point at the coast). As a result of refraction, close to shore the tsunami crests and troughs align with

Fig. 5 Simulated runup for scenarios S1887, SHyp and STot (Table 2) along the French Riviera. Acronyms are: TsM for Théoule sur Mer, MLN for Mandelieu la Napoule, PC for Pointe Croisette (in the city of Cannes), IL for Lerins Islands (part of the city of Cannes), AS for the beach Antibes la Salis (city of Antibes), CA for the Cape of Antibes, SLV for the city of Saint-Laurent du Var, AINCA for Aeroport International Nice Côte d’Azur, PN for the Port of Nice, CN for Cap de Nice, VLFR for the city of Villefranche-sur-Mer, SJCF for Saint-Jean Cap Ferrat, CF for Cap-Ferrat, BsM for Beaulieu-sur-Mer, CdA for Cap d’Ail, and RCM for Roquebrune-Cap-Martin. Red arrows correspond to focusing (converging) waves, green arrows are for defocusing (diverging) waves and blue arrows correspond to “neutral” behavior. Isobaths 20 m, 200 m and 500 m are plotted in white

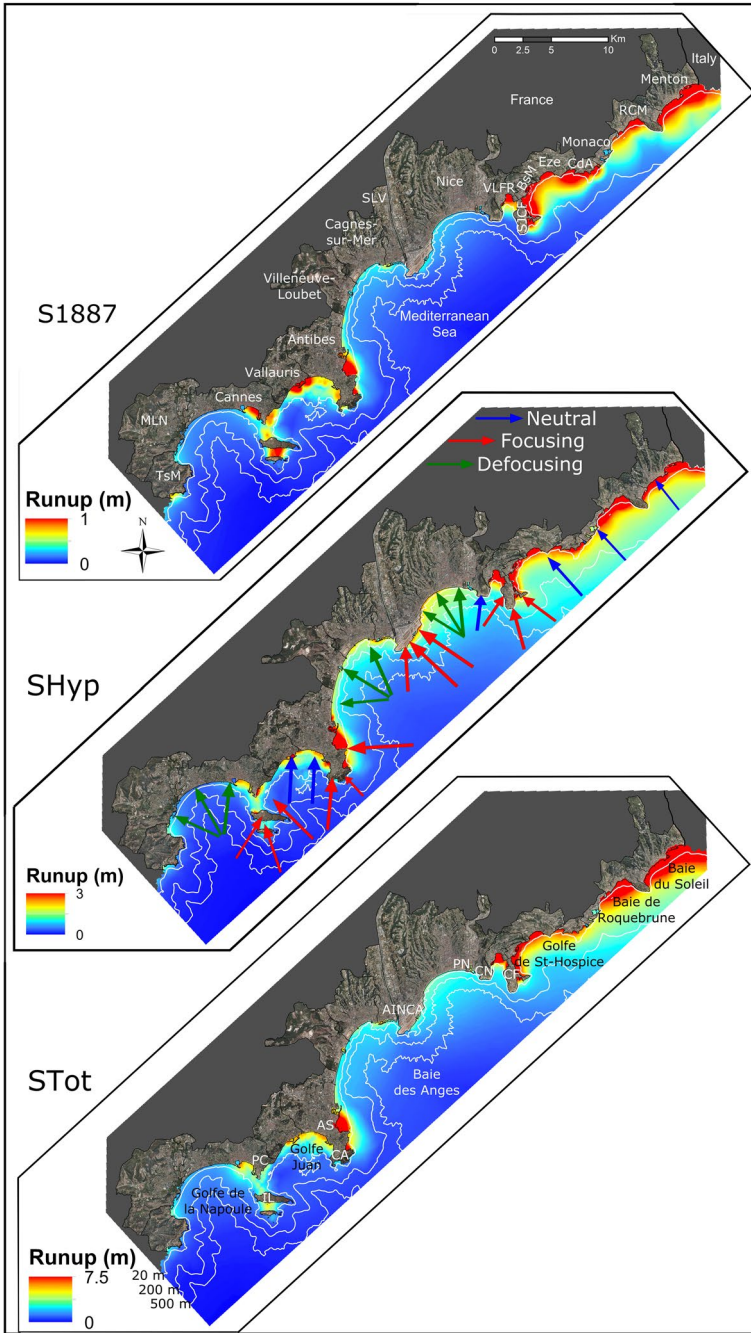
these isobaths, causing energy spreading in bays and energy focusing in between. This is illustrated in Fig. 5 for scenario Shyp, by green and red arrows. Where energy spreading (or defocusing) occurs, the tsunami is relatively attenuated, despite its amplification due to shoaling. This is the case for instance of: (1) the bay located between Théoule and Cannes, (2) that located between Antibes and Saint-Laurent-du-Var (western part of *Baie des Anges*), (3) the Bay of Nice (eastern part of *Baie des Anges*). Some bays, however, have a “neutral” behavior because the isobaths are straighter ahead of them (blue arrows on the same figure). We employ the word “neutral” to refer to straight isobaths (i.e., neither convex nor concave) whose shape does not affect the wave height through focusing or defocusing. This is the case of the bay located in between Cannes and Antibes and, approximately, of all those located in between Cap-Ferrat and Menton. In those “neutral” bays, wave amplification is due to other processes such as shoaling and wave directivity.

In contrast, on most headlands in between bays, the isobaths are concave and refraction causes the tsunami energy to focus on those, which combined with shoaling effects causes the largest predicted runups. Actual runup amplification, however, is function of the isobath curvature, and hence, the exact location of energy focusing area is difficult to anticipate, due to the complexity of the isobath geometry; it is not our scope here to cover these points in detail. Figure 5 shows that such amplification areas occur at *Cap d’Antibes*, off of Nice Côte d’Azur International Airport at the opposite side of the bay, *Cap Ferrat* and, to a certain extent, at Pointe-Croisette and Lérins Islands, which are shaped like a discontinuous headland. Finally, similar to bays, some headlands behave in a more neutral way because the isobaths surrounding them are fairly straight. This is the case for *Cap de Nice*.

Overall, in all the scenarios, the area in between *Cap de Nice* and Menton experiences the largest runups (Fig. 5), due to: (1) the north-northwestern tsunami directivity of the initial wave propagation east of *Cap de Nice*, since in all cases the longitudinal axis of the rupture area is much larger than the transverse one (Figs. 2, 4; Table 2); (2) using the Okada (1985) model, the largest deformations/surface elevations occur near the central line of the dislocation.

3.2 Overall maximum tsunami currents

Next we analyze tsunami current magnitudes in the coastal area where depth is less than 100 m deep (~55 fathoms). This would correspond to the mooring zone of boats (either at berth or using an anchor). Similar to Lynett et al. (2014) and BI-20, for each earthquake scenario, Fig. 6 shows the overall distribution of the maximum local tsunami current as a function of depth in this area. In the intensity scale introduced by Lynett et al. (2014), 1.50 m s^{-1} (3 knots) is the current threshold below which boats will not suffer tsunami damage. For the S1887, SHyp and STot scenarios, this threshold value approximately occurs at a 10 m (~6 fathoms), 20 m (~12 fathoms), and 35 m (~19 fathoms)



depth, respectively. Hence a safe distance/depth offshore that could be recommended in navigation guidelines in this area, for all 3 cases, is beyond the location of the 35 m isobath. Therefore, independently from the earthquake magnitude and likelihood for

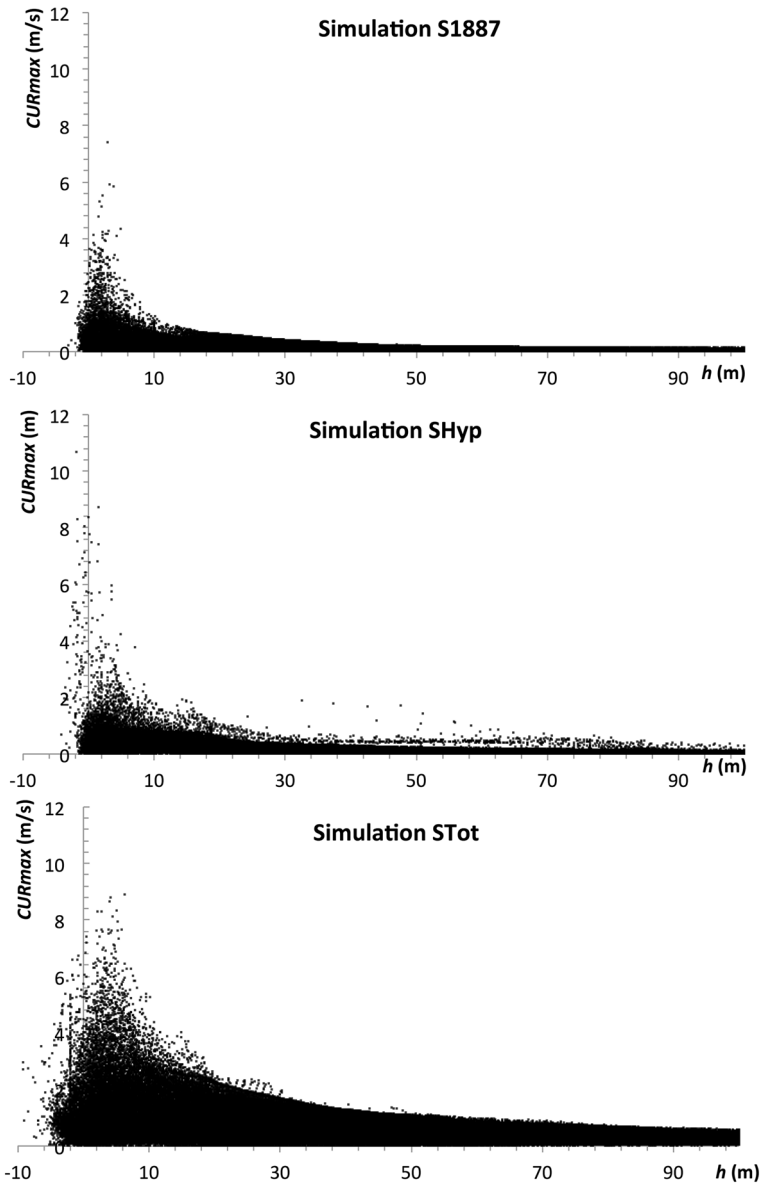


Fig. 6 Maximum tsunami induced current CUR_{max} for scenarios S1887, SHyp and STot (Table 2) along the French Riviera, as a function of water depth h from the coastline. Negative values of h correspond to inundated areas onland

tsunami generation, which may not be immediately determined or known, boats could sail away from shore to safe areas located beyond this water depth.

3.3 Relating maximum tsunami amplitudes and induced currents

Following BI-20, we analyzed the relationship between maximum tsunami amplitude H_{max} and induced currents CUR_{max} , in two areas: (1) from the coast to a 10 m depth (including inundated areas), and (2) from a 10 m to a 100 m depth (Fig. 7). These two areas correspond to distinct activities: the immediate vicinity of the coastline ($h < 10$ m) corresponds to occupied areas (populations, beaches, on land structures, marine/port structures, ships at berth), while farther away from shore, floating bodies (boats, buoys that could be anchored or not) are of greater concern. As seen above, this can also be the area where boats can escape since it is likely to be affected only by weaker currents.

The simple relationship (1) between the maximum currents CUR_{max} and amplitudes H_{max} based on linear long wave theory (g being the gravity acceleration and h the local water depth) (BI-20) is plotted in each of Fig. 7's panels, as two lines for $h = 10$ and 100 m.

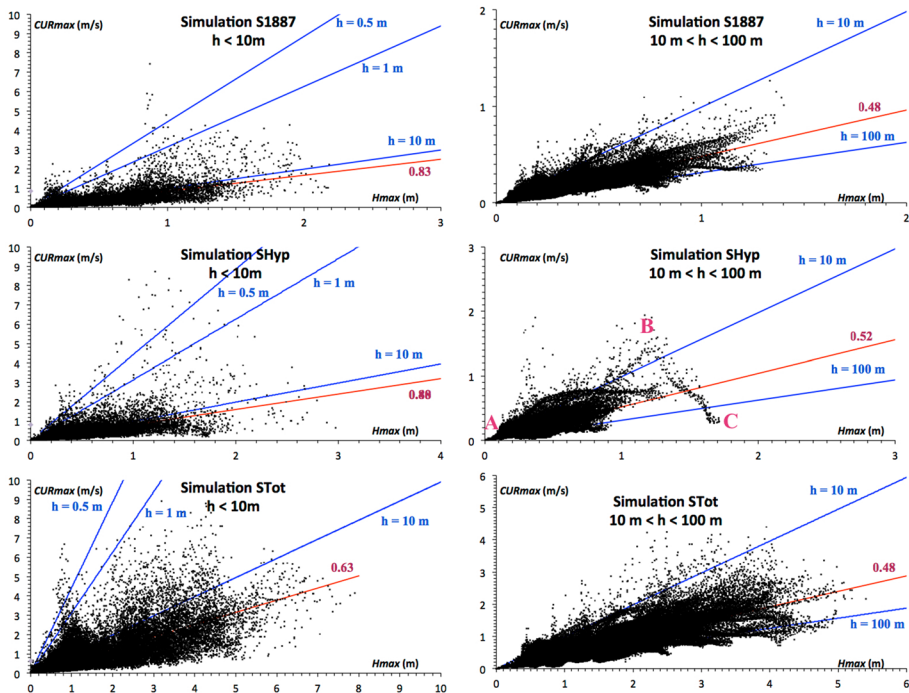


Fig. 7 Maximum simulated tsunami current (CUR_{max}) versus maximum tsunami amplitude (H_{max}) for scenarios S1887, SHyp and STot (Table 2). Left column: applied to grid points with water depths $h < 10$ m (including inundated points, for which water depth is negative); right column: for grid points with water depths $10\text{ m} < h < 100$ m. Estimates of the linear regression curves (if existing) are also plotted for information (in red). A few h -abacuses based on linear theory (Eq. (1) taken from Boschetti and Ioualalen 2019, submitted) are reported (in blue)

$$\text{CUR}_{\max} = (g/h)^{1/2} H_{\max}. \quad (1)$$

As noted by BI-20, for $10 \text{ m} < h < 100 \text{ m}$ and whatever the scenario considered, most of the simulated points (and their actual linear best fit) fall between the sector delineated by these two lines; in contrast, near the shore ($h < 10 \text{ m}$) both the simulated points and their best linear fit are outside this sector. The reason is as follows: as tsunami waves approach the coast and depth decreases, their height increases due to shoaling, while wavelength decreases; hence, wave steepness increases and wave propagation becomes more nonlinear. As a result, the relationship between H_{\max} and CUR_{\max} is no longer well predicted by linear wave theory. In some cases, the trend can even be opposite: for instance, for the simulation SHyp, a surprising negative slope is predicted in between points B and C in Fig. 7, for $10 \text{ m} < h < 100 \text{ m}$. These points are located in the Bay of Villefranche-sur-mer (Fig. 10e), where point A, also reported in Fig. 7, is positioned at the bay entrance. While waves are entering the bay from point A (at 100 m depth) to B (at an approximate 15 m depth), the slope is positive and follows more or less that predicted by linear theory. But from point B to C (10 m depth), the slope turns negative with CUR_{\max} decreasing with an increasing H_{\max} . We propose two possible explanations for this: (1) since waves become highly nonlinear, the negative slope can be due to the fact that CUR_{\max} and H_{\max} no longer occur simultaneously and thus the points in Fig. 7 are artifacts; (2) at the location of CUR_{\max} (see Fig. 10) the bay exhibits two special features: to the west, the entrance of the harbor named “La Darse” hosts a sharp peer, and to the east, the morphology of the coast reveals a tip at the beginning of the Cap-Ferrat. Both features are likely to generate locally strong currents through overland hydrodynamics that has been captured in our 40 m grid resolution simulation. Note that the same behavior of CUR_{\max} and H_{\max} is also predicted for S1887 and STot (Fig. 10) within the same bay. However, the negative slopes are not visible in Fig. 7 because they are hidden within the cloud of points near the origin.

Besides the already discussed site-specific refraction effects, other physical phenomena affect tsunami propagation, such as an increasing bottom friction as well as breaking, that all impact the maximum current magnitude near the shoreline. These nearshore effects confirm the need for performing nonlinear tsunami simulations to obtain accurate results nearshore, where the largest impact and potential damage can also be expected. In the present simulations, these and other processes cause the relationship between CUR_{\max} and H_{\max} to become quite complex nearshore and onshore, and difficult to anticipate a priori; hence, it is crucial to assess tsunami hazard separately through both variables. This point supports using an ad hoc tsunami intensity measure, such as proposed by BI-20, as detailed hereafter.

3.4 Detailed mapping of maximum tsunami amplitudes, induced currents, and corresponding tsunami intensity along the French Riviera

The denomination of “French Riviera” is only a literary reference, which is not geographical nor administrative. While it is bounded by the Italian border at its eastern side, its western border is not clear because it changes from one author to another. We take here the more restrictive definition for this area, that is, the French administrative district of the *Alpes-Maritimes*.

In the following, we more thoroughly assess overall tsunami hazard along the *Alpes-Maritimes* coast, by including other variables besides runup. As stated above, this will be achieved by simultaneously considering the maximum amplitude maps, currents, as well

as derived tsunami intensity maps. Like BI-20, we favor the tsunami amplitude maps over runup charts because, as previously mentioned, the latter do not explicitly provide the effective water column that is encountered by structures and persons, which is the basis for the proposed intensity scale. In addition, the flatter coastal areas (beaches) generally have an extent on the order of a few tens of meters, which happens to be close to our grid resolution of 40 m. For this reason, here we consider that the nearest sea point is a "beach" point whether there is flooding or not.

For clarity, the French Riviera is divided into three zones: the WEST zone extending from Théoule-sur-Mer to Antibes, the CENTER zone, from Villeneuve-Loubet to Beaulieu-sur-Mer, and the EAST area, from the city of Eze to the Italian border.

3.4.1 Tsunami hazard in the WEST part of the French Riviera

See Fig. 8.

3.4.1.1 Intermediate hazard scenarios S1887 and SHyp In general, for a magnitude lower than M_w 7, the Gulf of Napoule is not greatly exposed to tsunami hazard, with $H_{max} < 0.3\text{--}0.4$ m (Fig. 8a,b) and weak $CUR_{max} < 0.25$ m s^{-1} (Fig. 8d,e). As a result, the

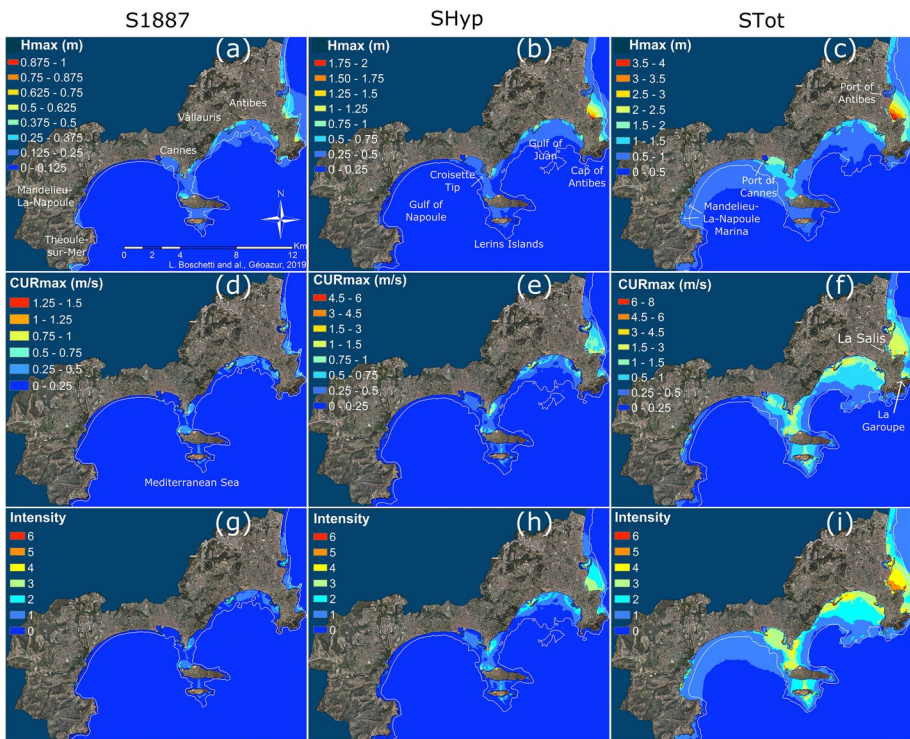


Fig. 8 Spatial distribution of the maximum wave amplitude H_{max} (a, b, c), maximum tsunami induced current CUR_{max} (d, e, f), and tsunami intensity as defined in Table 1 and Fig. 3 (g, h, i) for scenarios S1887, SHyp and STot, respectively, simulated for the western side of the district of the Alpes-Maritimes (the French Riviera). White curves represent isobaths 10 m for scenario S1887, 20 m for SHyp and 35 m for STot



Fig. 9 Coastal road between Mandelieu-la-Napoule and Cannes, bordered by the beach and the railway, view to the WSW (Courtesy of Google Map Inc.)

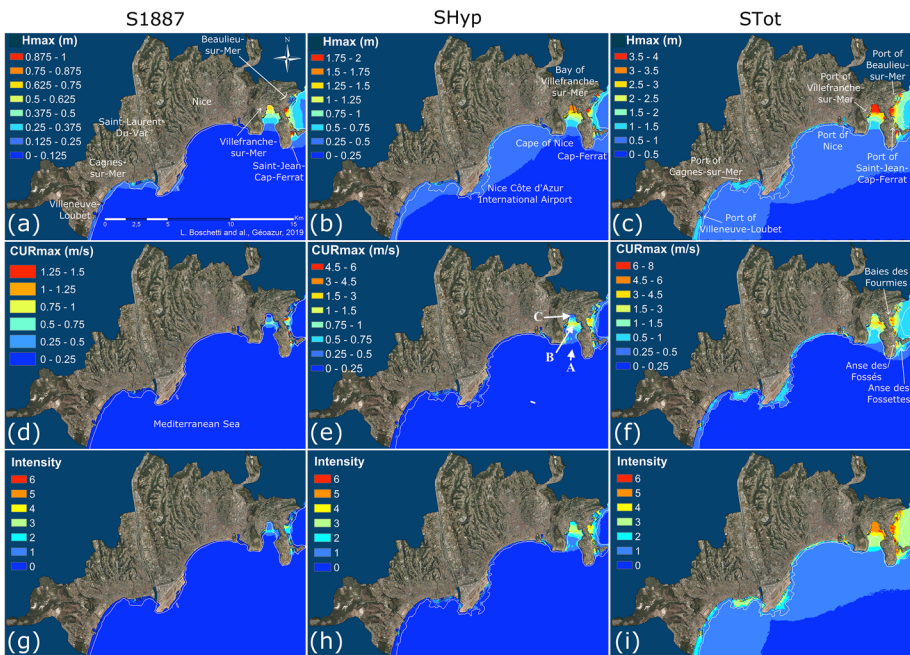


Fig. 10 Same as Fig. 8 for the central part of the District of the *Alpes-Maritimes* (the French Riviera)

tsunami intensity is negligible-to-weak (value of 0 for almost the whole sub-zone; Fig. 3 and 8g,h; Table 1). This is a sheltered subzone with little to no tsunami hazard. At the coast, no impact on people is expected. Immediately off the beach, there is no potentially dangerous movement to be expected from boats at berths or anchored.

To the east of port of Cannes, at Golfe Juan, including the Lerins Islands and as far as Antibes, H_{\max} values are disparate, ranging between 0.3 and 1.0 m, and locally reaching 1.5 to 2 m in the eastern area of *Cap d'Antibes* (beaches of *La Salis* and *La Garoupe*) for scenario SHyp (Fig. 8b). The beach of *La Salis* is flooded, as well as the street and storefronts on the opposite side. At the beach and shore, currents are generally less than 0.5 m s^{-1} , reaching up to 0.75 m s^{-1} at the *La Salis* and *La Garoupe* beaches. Corresponding tsunami hazard intensities are 3 or less (boats at berths are safe). At anchors, currents are generally lower than 1.50 m s^{-1} , with the exception of *La Salis* beach, where they can reach 3 m s^{-1} (Fig. 8e) and anchored boats could experience minor to moderate damage (intensity 3–4). Boats sailing away to the mouth of the small bay would be in sufficient depth to be sheltered (Fig. 8g,h, white line; Fig. 6).

3.4.1.2 Extreme hazard scenario STot In general, surface elevations less than 1 m and currents less than 0.5 m s^{-1} are simulated in the Gulf of *La Napoule* (Fig. 8c,f). The corresponding intensity is 1 (Figs. 3, 8i). This area consists of a large seaside zone frequented year-round by families of locals and tourists. The beach is at road level or below (accessed by stairs), depending on the portions. Most of the waterfront between Cannes and Mandelieu-la-Napoule consists in the parallel alignment of the beach, the littoral road and the rail track, standing about 2.5 m above the road (Fig. 9), thus blocking escape—only a few sparse pathways exist in the form of tunnels that could prove vulnerable to collapsing in case of an earthquake-generated tsunami or to flooding by the tsunami itself, should flooding reach beyond the seawall; the latter, however, is quite unlikely based on various scenarios considered here.

This geographic arrangement clearly affects coastal vulnerability and could yield a strong tsunami intensity, should a sufficiently large event occur. However, for our extreme event, the simulated tsunami impact is still small here ($H_{\max} < 1 \text{ m}$, $\text{CUR}_{\max} < 0.5 \text{ m s}^{-1}$) and intensity should not exceed 1. No flooding would result, and the road would remain a possible escape route. In contrast, The marina of Mandelieu la Napoule (wharf and anchorage) could experience flow depths up to 1.50 m at the coast (Fig. 8c) and currents up to 4.5 m s^{-1} (Fig. 8f). Intensity there could thus be much larger (3–4, Figs. 3, 8i), leading to potential loss of life and also to minor to moderate material damage to marine structures. The boats could possibly take shelter offshore to avoid harm; only a few hundred meters from shore would suffice (Fig. 8i, white line; Fig. 6).

Here, our results yield some possibly useful lessons. In practice, the evacuation of harbours would probably be a great challenge for such short notice events as those considered here, especially considering possible traffic jams to be expected in case of submersion. The identification of clear vulnerabilities and their communication to authorities should allow for a better preparedness of the communities. Moreover, during summer time, local harbours are packed with people and boats and, as a result, numerous ships and yachts are anchored nearby. Preparedness would also involve communicating with the crews of these boats.

The east of the city of Cannes, ranging from the old port to the entrance of the city of Vallauris, through the *Pointe Croisette* and the Lerins Islands, is subject to greater impact, mainly in the areas of anchorage. Here, tsunami amplitudes and currents could reach 2 m and 3 m s^{-1} , respectively, resulting in greater tsunami intensities: between 2 (causing little damage offshore) and 5 locally (significant damage to marine structures). *Golfe Juan* is impacted by amplitudes of up to 2 m. Although currents do not exceed 1 m s^{-1} at the beach, this still yields intensities up to 3, with significant human impact as a result. Farther

offshore, currents could reach 3 m s^{-1} at anchor, with corresponding intensities reaching 5–6, resulting in potentially major damage to boats. Boats would furthermore have to sail 3–4 km offshore to reach deep enough open sea areas and find shelter (Fig. 8i, white line; Fig. 7). In the event of a local co-seismic tsunami with immediate warning, our modelling predicts tsunami arrival times of 10–15 min after the earthquake. These distances and time are such that boat sheltering does not appear conceivable to us.

The tip of *Cap d'Antibes* is weakly impacted and does not experience significant flooding or currents. However, the eastern side of the cape is much more strongly impacted, with up to 4 m flow depth at the beach of *La Salis* and 2.50 m at that of *La Garoupe*. Currents are generally less than 3 m s^{-1} , but could locally reach $6\text{--}8 \text{ m s}^{-1}$ at anchor range, in both locations. Intensities therefore reach 5 for *La Salis* beach, both at anchor and at the beach. Moreover, this is the only area significantly flooded (up to 250 m inside the city), with high water levels and currents. This could cause catastrophic damage, first in terms of loss of life, due to large flow depths and, especially, currents, but also materially, with the destruction of waterfront businesses causing large moving debris loads that could in turn increase damage. The WEST part of this district therefore exhibits strong disparity in terms of flow depth, currents and therefore tsunami intensities, which results from the alternating focusing and neutral/defocusing areas of wave refraction along the coast (as discussed above).

3.4.2 Tsunami hazard in the CENTRAL part of the French Riviera

See Fig. 10.

3.4.2.1 Intermediate scenarios S1887 and SHyp From *Villeneuve-Loubet* to *Cape of Nice*, the calculated maximum amplitudes H_{\max} never exceed 0.75 m and, hence, no flooding is predicted (Fig. 10a,b). Maximum currents rarely reach 0.75 m s^{-1} (Fig. 10d,e). While H_{\max} may seem relatively insignificant, in areas where beaches are located below the littoral road at the toe of a several meter-high dike/seawall (e.g., *Castel Beach* in Nice, Fig. 11), escape paths may be up to several tens of meters away from many locations along the shore. Such



Fig. 11 Castel Beach, immediately east of the port of Nice, nearby the Old Town of Nice (Courtesy of Google Map Inc.). Red arrows represent beach exits

evacuation bottlenecks represent a factor of increased risk, keeping in mind that a 50 cm wave can prove fatal for children or elderly (Table 1). The widespread presence of pebbles increases this risk as it impedes running or quick walking on the beach. Farther East, *Cape of Nice*, which connects the port of Nice to that of Villefranche-sur-Mer, is a steep environment kept in its natural state. No beaches are found there but only small coves with periodic access paths to the sea, where one can quickly climb high enough above sea level. A pedestrian littoral path is also found there, which is sparsely frequented by hikers and fishermen. As a consequence, this zone poses little risk, owing both to the small expected tsunami flow depth and low vulnerability. Intensity ranges from 0 to 1 here (Fig. 10g,h), implying that this is a safe zone for boats to berth or anchor (Table 1). It is also worth noting that the Airport of Nice Côte d'Azur, a major international airport, is safe in terms of tsunami hazard as no flood is predicted there either.

From the bay of *Villefranche-sur-mer* to *Beaulieu-sur-mer*, including *Saint-Jean-Cap-Ferrat*, H_{max} can reach 1 m (scenario S1887) to 2 m (SHyp), without causing inundation albeit based on a 40 m resolution (Fig. 10a,b). At mooring, CUR_{max} is large, up to $0.75 \text{ m}\cdot\text{s}^{-1}$ for S1887 and $3 \text{ m}\cdot\text{s}^{-1}$ for SHyp (Fig. 10d,e). Significant intensities are therefore simulated for the harbor and port of *Villefranche-sur-Mer*, from 0 to 2 for S1887 and up to a level 4 for SHyp (Fig. 10g,h). The strongest intensities are at anchor. In the harbor, anchored yachts could potentially suffer significant damage if they were smashed onto berths. In this area, the road is located immediately next to the sea, along a dock. The beach of *Villefranche-sur-Mer*, for which an intensity of 1 for S1887 and 2 for SHyp are predicted, would be a shelter area for boats. Only a few spots with an intensity of 4 could potentially yield minor to moderate damage. The main beach is located at the bottom of the bay and laid out as a narrow strip, in between the sea and the rail tracks located just above it, atop a several meter-tall seawall against which waves would crash (Fig. 12). This geometry would likely cause people to be trapped as there are no evacuation routes here for several hundred meters, which would constitute a high vulnerability, especially in summer during daytime, when the area is typically very crowded.

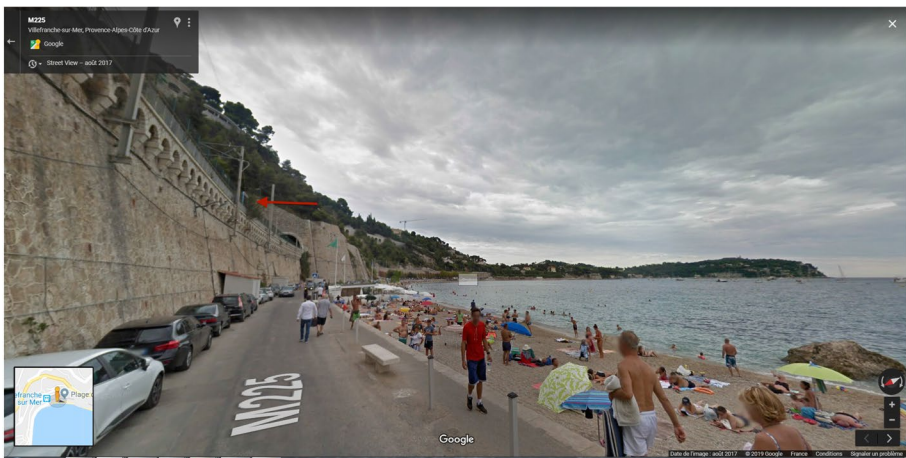


Fig. 12 The beach of Villefranche-sur-mer, at the foot of the railway station (Courtesy of Google Map Inc.). The red arrows locate the railway

The entire eastern part of *Cap-Ferrat*, including the *Anse des Fossés*, the *Anse des Fossettes*, the port of *Saint-Jean-Cap-Ferrat*, the *Baie des Fourmis* and the port of *Beaulieu-sur-Mer*, would be strongly impacted. Here H_{max} is always greater than 0.25 m for S1887 and in *Anse des Fossés* and the port of *Beaulieu-sur-Mer*, reaches the largest values found anywhere in the simulation of this scenario: 1 m. For the SHyp scenario, these values are 0.5–2 m (also in the port of *Beaulieu-sur-Mer*), but no flooding is predicted. Currents are generally greater than 0.25 m s^{-1} for S1887 and 0.5 m s^{-1} for SHyp, and can respectively reach 1.5 m s^{-1} and 3 m s^{-1} in bays and ports. This zone is thus classified from low (level 1) to high intensity (level 4) for these two scenarios. Once again, the mooring areas would experience larger currents and therefore higher intensities. The ports of *Saint-Jean-Cap-Ferrat* and *Beaulieu-sur-Mer* exhibit a very strong intensity, thus implying potentially significant damage.

3.4.2.2 Extreme scenario STot From *Villeneuve-Loubet* to the *Cape of Nice*, H_{max} almost always reaches values of 1.5–2 m without causing flooding (Fig. 10c). The simulated CUR_{max} are generally greater than 0.50 m s^{-1} and can occasionally reach 3 m s^{-1} at the mouth of the ports of *Villeneuve Loubet*, *Cagnes-sur-Mer* and *Nice* (Fig. 10f). Corresponding intensities are therefore generally intermediate on the littoral part (generally less than 3), thus implying a potentially significant impact on the population (Fig. 10i). In contrast, such intensities would have little impact on berthed and moored boats (Table 1). *Nice International Airport* is not flooded and is never threatened by such a tsunami.

The *Cape of Nice* and the southern and western parts of *Cap Ferrat* are subject to low to moderate intensities (levels 1 and 2) because CUR_{max} is less than 0.50 m s^{-1} and H_{max} is less than 1.5 m (Fig. 10c,f,i). On the other hand, in *Villefranche-sur-Mer*, at the port and at the beach, H_{max} is large, almost always higher than 2 m and up to 4 m at the beach or even at anchor. The same holds true for the coves located to the southeast (*anse des Fossés* and *anse des Fossettes*), the port of *Saint-Jean-Cap-Ferrat*, the *Baie des Fourmis* and the port of *Beaulieu-sur-Mer*. Currents are higher than 0.5 m s^{-1} over the entire zone, and can exceed 6 m s^{-1} at a few locations such as the mouth of the port of *Villefranche-sur-Mer*, the *Anse des Fossés*, the port of *Saint-Jean-Cap-Ferrat*, the port of *Beaulieu-sur-Mer* and the entry of the *Baie des Fourmis*. Intensities therefore range from moderate to strong (3–6) for the coastal part of these municipalities, with the largest values obtained at anchor. In the specific spots of *Villefranche Bay* (because of its particular shape), and east of *Cap Ferrat*, anchored boats should leave the entire area to be safe because the zone reaching an intensity of 4 (for which boats are damaged) extends offshore well beyond the usual bathymetry line of 35 m (Fig. 10i, white line).

3.4.3 Tsunami hazard in the EAST part of the French Riviera

The eastern side of the district, from Eze to Menton, is the closest to the earthquake epicenter, whatever the scenario, and is therefore potentially the most affected by the earthquake and tsunami waves. Wave directivity is responsible for the larger coastal flow depths found in this area, because the largest initial heights at the source occur just offshore of it (at least in the French Riviera, Fig. 4). This trend is increased as one approaches the Italian border.

3.4.3.1 Intermediate scenarios S1887 and SHyp Coastal tsunami amplitudes are less than 1 m for S1887 and less than 2 m for SHyp (Fig. 13a, b): *Eze* and *Cap-d'Ail* are impacted

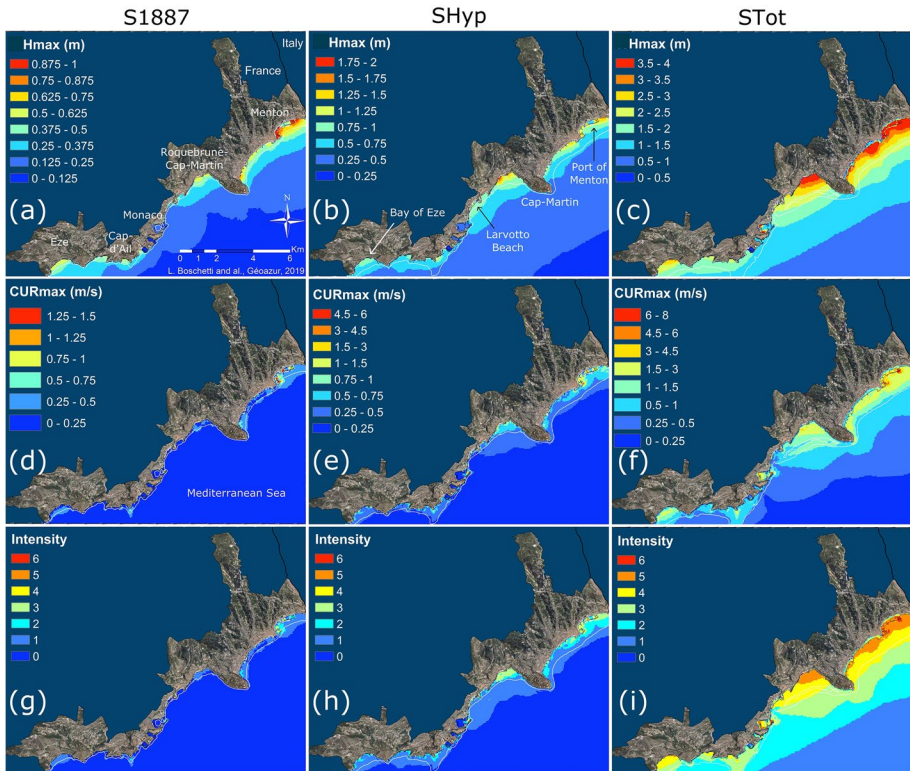


Fig. 13 Same as Fig. 8 for the eastern side of the District of the Alpes-Maritimes (the French Riviera)

by 0.25–0.6 m amplitudes for the first scenario, and 0.5–1 m for the second. Currents are generally less than 0.25 m s^{-1} , but can reach 0.5 m s^{-1} in some cases and are mainly on the order of 0.75 m s^{-1} in the first case, with values reaching 1 m s^{-1} locally in the second case (Fig. 13d, e). The respective intensities are therefore low (levels 0 and 1) and low to moderate (1–3) (Fig. 13g, h). Along the coast in this area, the shore is steep and roads do not run directly next to the sea, but higher up. Nevertheless, there are many beaches of varying width and distance to the road, which represent the sensitive part of this area, for the same reasons as those located further west, such as described above.

The *Principality of Monaco* is relatively protected and would suffer little impact in the first scenario, with wave amplitudes not exceeding 0.40 m and currents less than 0.25 m s^{-1} . The overall intensity for the city is therefore low (level 1). The second scenario would impact the city more, especially the beaches located at the eastern end of the city (Larvotto beach), with up to 1 m surface elevations and up to 1 m s^{-1} currents, thus conferring this area a moderate intensity (level 2). Overall, for both scenarios, the Principality of Monaco generally experiences low tsunami intensities. It is important though to keep in mind that the Principality is a vulnerable site, from a human standpoint (high population density) and because important economic assets are at stake in this wave focusing area.

The cities located further east, *Roquebrune-Cap-Martin* and *Menton*, are the most impacted in the entire district of *Les Alpes-Maritimes*, because of the tsunami directivity (see above). The *Bay of Roquebrune* would be potentially affected by flow depths reaching

0.75 m for S1887 and 2 m for SHyp at the coast. For these two scenarios, currents are respectively less than 0.5 m s^{-1} and 1.5 m s^{-1} , yielding intensities ranging from low in the first case (0 and 1) to moderate in the second case, due to stronger current effects. This coastal area consists mainly of beaches bordered by the railway. No road runs close to the sea. The littoral area is once again enclosed by a seawall with little escape routes available, making evacuation in the area very problematic. The southwestern part of *Cap Martin* is relatively sheltered in both scenarios. The entire *Bay of Roquebrune-Cap-Martin* up to the Italian border would be impacted by 0.5–1 m tsunami amplitudes for S1887, and 0.75–1.75 m for SHyp. In both cases, the largest values are observed on both sides of the port of *Menton*. In the S1887 scenario, currents are less than 0.5 m s^{-1} , but reach 1.5 m s^{-1} there. The SHyp scenario would generate currents ranging from 0.5 to 3 m s^{-1} , with a spatial distribution similar to the first one. In the S1887 scenario, the whole bay is therefore considered of low intensity (1–2), with again the exception of the port of *Menton*, where intensity is moderate to high (2–4). In the SHyp scenario, intensities are generally moderate (levels 2–4).

Although flow depth and currents are large, no flooding is predicted throughout this area. However, there are sensitive spots—beaches essentially—that can be heavily impacted and experience significant damage, mainly human. Some vulnerabilities need to be considered.

3.4.3.2 Extreme scenario STot This scenario appears to be severely impacting this coastal area. Unsurprisingly owing to the proximity of the source to the coast, the largest values in all our simulations are found here and for this scenario, for tsunami amplitudes, currents as well as flooding. *Eze* and *Cap d'Ail* could potentially be impacted by waves causing 1.50–3.5 m flow depth at the coast in the *Bay of Eze* (Fig. 13c). Currents would reach up to 3 m s^{-1} off the coast, being essentially less than 1 m s^{-1} on the coastal fringe (Fig. 13f). The corresponding intensities are thus strong to very strong (4 and 5), with similar values at beach and at anchor (Fig. 13i). The *Principality of Monaco* would also be impacted by significant waves, with amplitudes ranging between 1 and 4 m at the coast. The port of *Monaco* would experience the largest values, especially inside of it. This is also where the most important currents would be found, reaching up to 4.5 m s^{-1} , while these would be less than 1 m s^{-1} for the rest of the coast of *Monte Carlo*. *Larvotto beach* also appears to be heavily impacted in this scenario, with up to 3 m amplitudes and flooding of the beaches. Although currents are less than 1 m s^{-1} , this seaside area could experience disastrous consequences, particularly if this event occurred when it is crowded with families, as is the case in the summer season during daytime. The *Principality* is classified as medium to strong intensity (levels 2–6), mainly due to flow depths. Here again, intensities obtained at the beach and at anchor are similar.

The eastern end of the *Alpes-Maritimes* would be impacted by waves of great power, with maximum amplitudes generally exceeding 3 m, and currents greater than 1.5 m s^{-1} . Flooding would be important as well, resulting in very strong intensities, with flow depths reaching 2.5 m at the coast. This also holds for currents, whose expected extreme values could reach up to 6 m s^{-1} near port of *Menton* and decrease at the shore, down to 1.5 m s^{-1} . Corresponding intensities are thus high here, implying strong impact, between 4 and 5 over the whole coastal fringe, and decrease onland, following water level and current trends. Intensity remains large on the seaside, between 1 and 4, depending on location. A short distance offshore, the damage to anchored boats would be important, and the safe area for boats would stand at bathymetric depths exceeding 35 m (Fig. 13i, white line).

In summary, the eastern part of the French Riviera would be strongly impacted for the intermediate magnitude scenarios and very strongly impacted for the extreme one. Beaches once again would be the most sensitive areas, as many of these are enclosed between the sea and a steep shore (seawall or natural topography), which would pose problems for a timely evacuation and sheltering in case of a significant event occurring at a time of affluence (e.g., summer in daytime). The mooring areas also appear to be sensitive, as many of these are located at short distance offshore and would experience the highest wave amplitudes and strongest currents found in all our simulations. In the extreme scenario case, boats would have to move much further offshore to find shelter, which appears unlikely considering the short warning times. Note that boat damage would depend less on the season and time of the day the event would occur.

4 Discussion and conclusions

The French Riviera has been regularly affected by small to moderate seismicity, whose source is mostly located a few to a few tens of km offshore. In this context, the largest earthquakes would most likely be expected to occur and trigger tsunamis along the approximately 80 km long, active, North Ligurian Fault System (NLFS) (Eva et al. 2001; Bethoux et al. 1992; Larroque et al. 2011). At large recurrence time, although this remains poorly known and debated, the area could be affected by relatively large earthquakes such as the 1887 event, whose estimated magnitude was M_w 6.7–6.9, which caused an up to 2 m runup along the French Riviera (Larroque et al. 2012; Ioualalen et al. 2014). During this emblematic event, the 30–40 km-long eastern segment of the NLFS ruptured offshore of Imperia, Italy (similar to our scenario S1887; Larroque et al. 2012; Ioualalen et al. 2014). No other event of such a magnitude has been reported since antiquity, in spite of an arguably long documented time span here (Stucchi et al. 2012; Manchuel et al. 2017). However, the 1887 event proved that the occurrence of such large tsunamigenic events need to be considered along the NLFS, which has only recently been identified and documented and is still being studied. In particular, considering that the NLFS probably ruptures in segments and that its western segment has no evidence of a rupture equivalent to 1887 in historical times, our considered scenario SHyp is quite plausible for a future event. Likewise, fault systems are known for rupturing with varying patterns throughout seismic cycles, possibly alternating piecewise ruptures, such as S1887 and SHyp scenarios, and larger multiple-segment events, such as our STot scenario, which would rupture the whole NLFS with an estimated M_w 7.5 earthquake. Such a large event is thus also in the realm of possible future extreme events along the NLFS (Larroque et al. 2012; Ioualalen et al. 2014). Although most likely very rare (with possibly thousands of years in recurrence time), the possibility of such an event can thus not be ruled out, hence our analysis of this extreme scenario in the present study.

Following Ioualalen et al. (2014) and Nemati et al. (2019), we favored a deterministic approach to reassess the regional tsunami hazard based on three scenarios that were built from up-to-date knowledge of the seismotectonics and morphology of the area. Note that understanding the seismotectonics of the area is still work in progress and there is no unambiguous estimate for the return periods of large earthquakes such as those considered in this study; hence, there is no reliable estimate for local tsunami return periods either. It should be noted that, unlike the two others, the magnitude of STot extreme scenario is not supported by historical or paleo-seismological data and simply stems from the sheer size

of the rupture zone if it were to be activated as part of a single event. Note, however, once again, there is no conspicuous evidence to date that such a complete rupture of the NLFS should be ruled out; the absence of any structural discontinuity in the surface traces of the NLFS actually points to the opposite. We have therefore decided to consider this maximalist scenario, even if its occurrence is likely quite rare at best, in order to establish an upper bound of the expected tsunami hazard along the French Riviera. Finally, we consider that these 3 scenarios based on historical and tectonic data are sufficient to deterministically analyze coseismic tsunami hazard in this region.

In this respect, Ioualalen et al. (2014) performed an initial mapping of tsunami coastal hazard using the *FUNWAVE* tsunami propagation model to simulate a variety of scenarios in a coarse 100 m grid. Such a resolution, while adequate offshore was too coarse along the coast. More recently, Nemati et al. (2019) refined these computations using *FUNWAVE-TVD* in a series of nested grids of varying resolution. Their finer nested grids had 40 m and 10 m resolutions. They showed in particular how complex coastal areas such as Nice's harbors were clearly under-resolved in earlier modeling, leading to significantly over-estimated runup values. Moreover, they used a new set of high-resolution bathymetric data, obtained from multibeam surveys, which in particular improved accuracy over the poorly documented continental shelf on the French side of the *Riviera*. In the present study, which aims at assessing tsunami intensity, while we still used a single grid with *FUNWAVE* (as in Ioualalen et al. 2014), its 40 m grid resolution allowed for a sufficient description of most coastal features. Although not shown in Nemati et al. (2019), our present results were compared with theirs and their basic statistics are very similar.

In terms of tsunami hazard assessment and warning, the main criteria are the polarity and amplitude of the first incoming wave, as well as the arrival time, which here depend on the considered NLFS rupture scenarios. Our analysis of the first wave indicates a very short arrival time, only a few minutes being needed to reach the French Riviera coast, whatever the scenario. On such short notice, the warning conditions will be poor. Additionally the polarity of the wave (crest vs. trough arriving first) is not systematic so, this will also affect warning conditions. Moreover, as seen above, even if a trough led the wave train, it could be imperceptible, making for a poor warning indeed. Hence, feeling the earthquake and reacting accordingly based on pre-existing instructions (e.g., head for high ground) is arguably the most reliable warning and mitigation measure for the possible tsunamis in this area.

We always learn from benchmarks between different studies involving various numerical models or source scenarios. The main element of comparison is the spatial variability of the tsunami magnitude (surface elevation and current) at the coast. This parameter is crucial for improving the preparedness of a given coastal area to the expected hazard. On a first-order basis, for any given tsunami propagation, the shoaling effect (the slope effect) applies everywhere in the same way, so that alone it cannot explain the spatial variability of the coastal tsunami height, especially when applying the elementary $\frac{1}{4}$ -powered Green's law which has been established through many assumptions (very long linear, non-dispersive and conservative waves, energy flux conservation mainly). The question is thus: are the other amplification (or attenuation) processes able to generically describe such variability, such as, focusing/defocusing, resonance, wave directivity, etc.? Some of these depend on coastal morphology and bathymetry (e.g., focusing/defocusing), which are good candidates because they are independent of the tsunami itself. Others (wave directivity, resonances among them) are less generic; for example, resonance depends on the tsunami frequency content and wave directivity depends on the geometry and dynamics of the sea-floor deformation.

To visually illustrate this issue, we have always normalized the H_{\max} color scale for each scenario. As a result whatever the scenario, figures look similar to the first-order because the focusing/defocusing effect is usually the leading amplification/attenuation process of tsunami amplitude and current (e.g., Figs. 8, 10, 13). When looking more closely, there are differences when changing earthquake scenarios. Our deterministic approach, based on physical rupture scenarios, intends to directly provide magnitude maps. Other studies have tried to estimate empirically this spatial variability. Gailler et al. (2018) and Glimsdal et al. (2019), in an effort to provide fast estimates of the tsunami wave height for an operational warning system purpose, applied the empirical β -coefficient that was proposed by Reymond et al. (2012) and Jamelot and Reymond (2015) to the French Riviera. This coefficient is included in their extended Green's law. For each considered coastal area, a β -spatial distribution must be estimated empirically through an ensemble of numerical simulations, which makes it semi-generic. As a result, in their French Riviera case study, the more detailed the β -spatial distribution, the more accurate and quickly computed the tsunami coastal distribution. It is also fair to say that the distribution depends on the scenario, which is not surprising since the amplification/attenuation of the wave also depends on the wave characteristics as said above. For example, a spatial distribution of the β coefficient better estimates the spatial tsunami distribution compared to a uniform one within the bay of Villefranche-sur-mer. This is because their coefficient varies with the bay morphology. It is also noticeable that some differences appear when changing scenario, likely due to the differences between the entering wave characteristics as said above. For example, the wave height is larger at the breakwater protecting the harbor than at the beach, which is consistent with their derived β -amplifying coefficient values of 1.2 and 0.6, respectively, for their Djjelli 1856 scenario J7.1, which is excellent. However, their local scenario L, which is supposed to represent the 1887 event, using different rupture parameters than ours, provides similar wave heights at the same locations. However, in our simulation, the maximum wave height is greater at the beach (Fig. 10b) probably because our rupture parameters are different, which suggests that the characteristics of the incoming wave also play a significant role, in addition to that of coastal morphology.

Our deterministic approach for estimating extreme tsunami hazard complements others that can be considered semi-probabilistic. Our procedure proposes a global tsunami mapping that can be exploited for preparedness. The approach of Gailler et al. (2018), that is discussed above, may be considered as semi-probabilistic since both deterministic source scenarios are considered and stochastic regression laws are estimated in order to represent at best the local site effects. Once the local laws are prescribed (for wave heights in their case), they can be integrated in a warning system protocol such as operated by the French CENALT (*Centre National d'ALerte aux Tsunamis*) (Schindel el et al. 2015), which is a component of the regional NEAMTWS (North East Atlantic and Mediterranean Tsunami Warning System). The CENALT uses more than 2000 pre-computed source scenarios for the Western Mediterranean. Based on this database and the estimated local regression laws, a tsunami hazard mapping can be performed at very low CPU and memory costs. Hence, for an actual event, the tsunami mapping associated with the earthquake source parameters is extracted from the database and a more accurate mapping is issued based on the local regression laws in near real time (hopefully before the first wave arrival which is only a few minutes in the case of our local sources). Eventually, the regression laws may be post-processed or possibly included in the data base mapping. It is fair to say that our methodology consisting in the mapping of the intensity may possibly enrich CENALT's if the latter approach was extended to include tsunami-induced currents and, ultimately, an intensity scale such as proposed by BI-20.

Following Nemati et al. (2019)'s mapping of runup along the French Riviera, the present tsunami intensity study is the next necessary step to be able to assess coastal vulnerability and resilience in future studies. Results of simulations of coastal runups, maximum tsunami depths, and currents reported by Nemati et al. (2019) and in the present study, along with the proposed estimates of potential damage analyzed here, may be used to design mitigation plans that could help preparing local populations, improve the resiliency of littoral structures, as well as draw plans for relevant emergency responses to tsunami hazard.

Our mapping of tsunami intensity reveals a high spatial variability of potential damage that is mainly related to site-specific effects (e.g., wave energy focusing vs. neutral or defocusing processes), to tsunami directivity, and earthquake source location. Nemati et al.'s (2019) as well as our study allow assessing how areas of the French Riviera should be classified with respect to tsunami hazard, from "sheltered" to "highly exposed," through mapping of the inundation and tsunami current fields: capes (*Cap d'Antibes* and *Cap Ferrat*) along with semi-enclosed bays (e.g., *La Salis Beach* at Antibes) would be faced with amplified waves. In contrast, widely opened bays (e.g., *Baie des Anges* and *Baie de Cannes*) would be less exposed due to wave defocusing. The latter areas turn out to be the most densely developed, with the higher population concentrations, especially at summer time.

However, such statements are quite general and some more local insight was needed, which was the purpose of this study: once the tsunami magnitude is derived (by combining the maxima of amplitudes and currents), potential damage estimates can be derived from the tsunami intensity scale of BI-20.

Acknowledgements L. Boschetti, M. Ioualalen and J.-X. Dessa acknowledge support from: (1) the European Commission under the project "Assessment, STRategy And Risk Reduction for Tsunamis in Europe," ASTARTE (Grant No. 603839) and (2) the French government, through the UCA-JEDI Investments in the Future project managed by the National Research Agency (ANR) with the reference number ANR-15-IDEX-01. F. Nemati and S. Grilli acknowledge support for this work from the US National Science Foundation Grant CMMI-15-35568. Finally, the authors acknowledge with appreciation one anonymous reviewer who helped improve the first draft of the manuscript.

References

- Alasset PJ, Hébert H, Maouche S, Calbini V, Meghraoui M (2006) The tsunami induced by the 2003 Zemmouri earthquake (MW = 6.9, Algeria): modelling and results. *Geophys J Int* 166:213–226. <https://doi.org/10.1111/j.1365-246X.2006.02912.x>
- Béthoux N, Fréchet J, Guyoton F, Thouvenot F, Cattaneo F, Nicolas M, Granet M (1992) A closing Ligurian sea. *Pure Appl Geophys* 139:179–194
- Boschetti L, Ioualalen M (2019) Integrated tsunami intensity scale based on maxima of tsunami amplitude and induced current. *Natural Hazards*, submitted as a companion paper
- Denza F (1887) *Alcune notizie sul terremoto del 23 febbraio 1887*. Torino
- Déverchère J, Yelles K, Domzig A, Mercier de Lépinay B, Bouillin J, Gaullier V, Bracène R, Calais E, Savoye B, Kherroubi A, Le Roy P, Pauc H, Dan G (2005) Active thrust faulting offshore Boumerdes, Algeria, and its relations to the 2003 Mw 6.9 earthquake. *Geophys Res Lett* 32(4):L04311. <https://doi.org/10.1029/2004GL021646>
- Eva C, Rabinovich AB (1997) The February 23, 1887 tsunami recorded on the Ligurian coast, western Mediterranean. *Geophys Res Lett* 24:2211–2214
- Eva E, Sollarino S, Spallarossa D (2001) Seismicity and crustal structure beneath the western Ligurian Sea derived from local earthquake tomography. *Tectonophysics* 339:495–510. [https://doi.org/10.1016/S0040-1951\(01\)00106-8](https://doi.org/10.1016/S0040-1951(01)00106-8)

- Ferrari G (1991) The 1887 Ligurian earthquake: a detailed study from contemporary scientific observations. *Tectonophysics* 193:131–139
- Glimsdal S, Lovholt F, Harbitz CB, Romand F, Lorito S, Orefice S, Brizuela B, Selva J, Hoechner A, Volpe M, Babeyko A, Tonini R, Wronna M, Omira R (2019) A new approximate method for quantifying tsunami maximum inundation height probability. *Pure Appl Geophys* 176:3227–3246. <https://doi.org/10.1007/s00024-019-02091-w>
- Grilli ST, O'Reilly C, Harris JC, TajalliBakhsh T, Tehranirad B, Banihashemi S, Kirby JT, Baxter CDP, Eggeling T, Ma G, Shi F (2015) Modeling of SMF tsunami hazard along the upper US East Coast: Detailed impact around Ocean City MD. *Nat Hazards* 76(2):705–746. <https://doi.org/10.1007/s11069-014-1522-8>
- Gailler A, Hébert H, Schindelé F, Reymond D (2018) Amplification laws for the French tsunami warning center: numerical modeling and fast estimate of tsunami wave along the French Riviera. *Pure Appl Geophys* 175:1429–1444
- Ioualalen M, Migeon S, Sardoux O (2010) Landslide tsunami vulnerability in the Ligurian Sea: case study of the 1979 October 16 Nice international airport submarine landslide and of identified geological mass failures. *Geophys J Int* 181(2):724–740
- Ioualalen M, Larroque C, Scotti O, Daubord C (2014) Tsunami mapping related to local earthquakes on the French–Italian Riviera (western Mediterranean). *Pure Appl Geophys* 171(7):1423–1443
- Jamelot A, Reymond D (2015) New tsunami forecast tools for the French Polynesia tsunami warning system. Part II: numerical modeling and tsunami height estimation. *Pure Appl Geophys* 172(3–47):805–819
- Lambert J, Terrier M (2011) Historical tsunami database for France and its overseas territories. *Nat Hazards Earth Syst Sci* 11:1037–1046
- Larroque C, Béthoux N, Calais E, Courboux F, Deschamps A, Deverchère J, Stéphan JF, Ritz JF, Gilli E (2001) Active and recent deformation at the Southern Alps-Ligurian basin junction. *Neth J Geosci Geologie en Mijnbouw* 80:255–272
- Larroque C, Delouis B, Godel B, Nocquet J-M (2009) Active deformation at the southwestern Alps-Ligurian basin junction (France-Italy boundary): evidence for recent change from compression to extension in the Argentera massif. *Tectonophysics* 467:1–4. <https://doi.org/10.1016/j.tecto.2008.12.013>
- Larroque C, Mercier de Lépinay B, Migeon S (2011) Morphotectonic and fault-earthquake relationships along the northern Ligurian margin (Western Mediterranean) based on high resolution multibeam bathymetry and multichannel seismic-reflection profiles. *Mar Geophys Res* 32:163–179. <https://doi.org/10.1007/s11001-010-9108-7>
- Larroque C, Scotti O, Ioualalen M (2012) Reappraisal of the 1887 Ligurian earthquake (western Mediterranean) from macroseismicity, active tectonics and tsunami modelling. *Geophys J Int*. <https://doi.org/10.1111/j.1365-246X.2012.05498.x>
- Lynett PJ, Borrero J, Son S, Wilson R, Miller K (2013GL) Assessment of the tsunami-induced current hazard. *Geophys Res Lett* 41:2048–2055. <https://doi.org/10.1002/2013GL058680>
- Manchuel K, Traversa P, Baumont D, Cara M, Nayman E, Durouchoux C (2017) The French seismic CAtalogue (FCAT-17). *Bull Earthq Eng*. <https://doi.org/10.1007/s10518-017-0236-1>
- Nemati F, Grilli ST, Ioualalen M, Boschetti L, Larroque C, Trevisan J (2019) High-resolution coastal hazards assessment along the French Riviera from coseismic tsunamis generated in the Ligurian fault system. *Nat Hazards*. <https://doi.org/10.1007/s11069-018-3555-x>
- Okada Y (1985) Surface deformation due to shear and tensile faults in a half-space. *Bull Seismol Soc Am* 75(4):1135–1154
- Papadopoulos GA (2003) Quantification of tsunamis: a review. In: Yalçiner AC, Pelinovsky E, Okal E, Synolakis CE (eds) *Submarine landslides and tsunamis, nato science series (Series IV: Earth and environmental sciences)*, vol 21. Springer, Dordrecht. https://doi.org/10.1007/978-94-010-0205-9_30
- Papadopoulos GA, Imamura F (2001) A proposal for a new tsunami intensity scale Internat. In: *Tsunami symposium 2001 proceedings* Seattle, Washington, pp 569–577
- Pophet N, Kaewbanjak N, Asavanant J, Ioualalen M (2011) High grid resolution and parallelized tsunami simulation with fully nonlinear Boussinesq equations. *Comput Fluids* 40:258–268
- PPFR (1999) *Plans de prévention des risques naturels (PPR)—Risques d'inondation—Guide méthodologique*. La documentation Française, p 126, ISBN: 2-11-004402-0
- PPFR-Thau (2012) *Plan de prévention des risques naturels d'inondation—Bassin versant de l'Etang de Thau, Commune de Villeveyrac*. Direction Départementale des Territoires et de la Mer – Service Eau et Risques, Préfecture de l'Hérault, p 54
- Reymond D, Okal E, Hébert H, Bourdet M (2012) Rapid forecast of tsunami wave height from a data base of pre-computed simulations, and application during the 2011 Tohoku tsunami in French Polynesia. *Geophys Res Lett* 30(11):L11603

- Sahal A, Roger J, Allgeyer S, Lemaire B, Hébert H, Schindelé F, Lavigne F (2009) The tsunami triggered by the 21 May 2003 Boumerdès-Zemmouri (Algeria) earthquake: field investigations on the French Mediterranean coast and tsunami modelling. *Nat Hazards Earth Syst Sci* 9:1823–1834. <https://doi.org/10.5194/nhess-9-1823-2009>
- Schambach L, Grilli ST, Kirby JT, Shi F (2018) Landslide tsunami hazard along the upper US East Coast: effects of slide rheology, bottom friction, and frequency dispersion. *Pure Appl Geophys*. <https://doi.org/10.1007/s00024-018-1978-7>
- Schindelé F, Gailler A, Hébert H, Loevenbruck A, Gutierrez E, Monnier A, Roudil O, Reymond D, Rivera L (2015) Implementation and challenges of the tsunami warning system in the western Mediterranean. *Pure Appl Geophys*. <https://doi.org/10.1007/s00024-014-0950-4>
- Shuto N (1991) Tsunami intensity and disasters. In: Tinti S (ed) *Tsunamis in the World*. Kluwer Academic Publishers, Dordrech, pp 197–216. https://doi.org/10.1007/978-94-017-3620-6_15
- Stucchi M, Rovida A, Gomez-Capera AA et al (2012) The SHARE European earthquake catalogue (SHEEC) 1000–1899. *J Seismol*. <https://doi.org/10.1007/s10950-012-9335-2>
- Taramelli T, Mercalli G (1888) Il terremoto ligure del 23 febbraio 1887. *Annali dell'Ufficio Centrale Meteorologico e Geodinamico Italiano* II 8(4):331–626
- Tehrani-rad B, Harris JC, Grilli AR, Grilli ST, Abadie S, Kirby JT, Shi F (2015) Far-field tsunami impact in the north Atlantic basin from large scale flank collapses of the Cumbre Vieja volcano La Palma. *Pure Appl Geophys* 172(12):3589–3616. <https://doi.org/10.1007/s00024-015-1135-5>
- Tinti S, Maramai A, Graziani L (2004) The new catalogue of Italian tsunamis. *Nat Hazards* 33:439–465
- Wei G, Kirby JT (1995) A time-dependent numerical code for extended Boussinesq equations. *J Waterw Port Coast Ocean Eng* 121:251–261
- Wei G, Kirby JT, Grilli ST, Subramanya R (1995) A Fully Nonlinear Boussinesq model for surface waves. Part1. highly nonlinear unsteady waves. *J Fluid Mech* 294:71–92
- Wells DL, Coppersmith KJ (1994) New empirical relationships among magnitude, rupture length, rupture width, rupture area, and surface displacement. *Bull Seismol Soc Am* 84(4):974–1002

Publisher's Note Springer Nature remains neutral with regard to jurisdictional claims in published maps and institutional affiliations.